OMAE2022- 79607

RESPONSE MITIGATION OF FLOATING PLATFORM BY POROUS-MEDIA TUNED LIQUID DAMPERS

Wen-Huai Tsao[1]
Department of Civil and Environmental Engineering, Louisiana State University
Baton Rouge, USA

Ying-Chuan Chen[2]
KBR
Houston, USA

Christopher E. Kees[3]
Department of Civil and Environmental Engineering, Louisiana State University
Baton Rouge, USA

Lance Manuel[4]
Department of Civil, Architectural and Environmental Engineering, The University of Texas at Austin
Austin, USA

ABSTRACT

A porous-media tuned liquid damper (PMTLD) can serve as an eco-friendly, economical, and effective dynamic vibration absorber. Placing porous media within a water tank can improve the capacity for energy dissipation and optimize the performance by varying its material properties. The numerical simulations of the floating platform dynamics in waves coupled with the sloshing problem in PMTLD are emphasized. Two numerical methods are adopted for fluid computation. The first potential-based approach employs a mixed-type boundary value problem (BVP) solver, which is implemented by the boundary element method (BEM), coupled with a free surface particle tracker, which includes the nonlinear damping effects via a quadratic Forchheimer term for PMTLD. Another equivalent mechanical model is also used exclusively for solving the linear PMTLD. The coupling behavior between fluid and structure is solved by the Newmark method. The second viscous approach uses the finite element method (FEM) to spatially discretize the Navier-Stokes equations and handles the free surface via the volume of fluid (VOF) and the level set (LS) equations. The multiphase simulation is implemented by a computational modeling toolkit Proteus for the fluid phase and Chrono for the solid phase. The correlations between potential flow and Navier-Stokes (NS) models are presented. The PMTLD is designed for a floating platform by analogy with the tuned mass damper (TMD). Numerical results show that the PMTLD can effectively reduce the structure's dynamic response in terms of vibration amplitude around resonance. Such damping devices have great potential for practical applications in offshore platforms and wind turbine design.

Keywords: Porous media; Tuned liquid damper; Equivalent mechanical model; Computational fluid dynamics; Fluid-structure interaction; Floating platform.

1. INTRODUCTION

In the new era of renewable energy, people seek economical and clean resources from the ocean so the marine industry grows rapidly. Various kinds of offshore platforms have been created and served as the work station for petroleum extraction, wind turbines, wave energy converters, and offshore fishery. In the ocean environment, they are subject to many kinds of loading such as wind, wave, current, ice, and earthquake. These disturbances will result in tremendous vibration that not only harms the seakeeping performance but also the longevity, even breaking the integrity. Therefore, vibration control technology is essential for offshore platforms. Due to the complexity of the floating body dynamics, the coupling effect brings unpredictable motions to the entire system. A single type of vibration absorber does not suit all purposes. Furthermore, it is difficult to monitor the motion of the platform. Therefore the vibration control for a floating structure remains challenging nowadays.

Typical floating structures, such as liquefied natural gas (LNG) vessels, floating storage regasification units (FSRU), floating production systems (FPS), and wind turbines, have special dynamic characteristics, so different devices are applied. For the ships, the rolling motion is the most concerned because the damping from the ambient fluid is usually too small to constrain its amplitude, especially when resonance occurs. A common solution is to equip the bilge keels on the hull to increase the hydrodynamic resistance and damping from the vortex [1]. An anti-rolling tank (ART), which consists of two vertical ducts connected at the bottom with a horizontal duct, distributed along the centerline of the ship is another effective damper for rolling reduction. Such liquid damper is also called tuned liquid column damper (TLCD) in structural engineering. Their active controllers have been implemented by installing propellers or pumps in the middle of the bottom tank [2-4]. Floating stations, such as fixed platforms, compliant towers, moored tension leg

platforms, floating production systems, have been equipped with dampers to reduce vibrations. TMD is one of the earliest solutions. It is an auxiliary mass attached to the main structure through springs and dashpot elements. It generates an out-of-phase control force against the external excitations and dampens the kinetic energy of the main structure. Once it is tuned to the resonant frequency, its performance can be maximized. Gattulli and Ghanem [5] applied active mass damper to reduce the vortex-induced vibration of offshore structures. Kawano [6] investigated the optimal control scheme of the semi-active TMD applied in a jack-up offshore platform. The TLCD had been also applied to the tension-leg platform (TLP). The effect on the roll and pitch motions reduction had been tested numerically and experimentally [7]. Due to the increasing demand for wind energy in recent decades, a race toward the gigantism of wind turbines has begun. Larger wind turbines become more flexible (due to mass reduction) but meanwhile have to bear higher loads. Besides, the rotating blades produce significant gyroscopic effects that interact with the platform's yaw and pitch. Other complicated phenomena like wind turbulence and shear, tower shadow, and wake effect from the neighboring turbines also occur. Many researchers took advantage of the aeronautics technologies to reduce the loads on wind turbines, such as blade pitch control [8], movable flaps on the trailing edge [9, 10]. In the area of structural engineering, most researchers had applied TMD, tuned liquid dampers (TLD), magnetorheological (MR) fluid damper, and other energy sinks [11] on the tower, nacelle or blade. Several TMD optimizations have been proposed [12, 13]. The multi-TMD system had been developed to reduce the sway motion of the nacelle [14]. Colwell and Basu [15] carried out the fatigue analysis and showed that TLCD can reduce the bending moment of the tower and extend the fatigue life. Tong et al. [16] designed a bidirectional TLD system located on the barge to reduce the load on the tower base. Chen et al. [17] used several spherical TLDs for better performance against seismic excitations. Martynowicz [18, 19] studied the controllable MR damper, which is a shock absorber equipped with electrical windings to generate a magnetic field and change the viscosity of the magnetic fluid, to alleviate the bending of the tower. Staino et al. [20] proposed a new system that consists of tendons and actuators embedded inside the blade to control the edgewise vibration. Among all the solutions, TMD is popular for several reasons. The design procedure is simple; it is easy to add in or remove from an existing system; its dynamic characteristics are suitable for the ocean environments. TLD could be more attractive since it requires lower construction costs and maintenance. However, its lack of inherent damping cripples its performance and the nonlinear behavior sometimes leads to mistuning easily [21]. Past researchers had proposed some solutions to enhance its damping effect by adding some internal obstructions, such as wall baffles [22] and screens [23]. Although many researchers have successively analyzed their performance [24-26], the entire progress to the practical application remains stagnant. In recent years, another new type of TLD had been invented by installing porous media inside the water tank [27, 28]. The porous media can bring a higher capacity for energy dissipation. The equivalent mechanical model was proposed

to design the PMTLD by analogy with TMD. Tsao and Chang [29] completed the supplementary solutions of the linear model and carried out the experimental verification on the associated dynamic characteristics change. Tsao and Huang [30] included the quadratic damping equation in the numerical method and determined some essential parameters from resonant experiments. Tsao et al. [31] obtained the nonlinear damping ratio from the resonance experiments. The results showed that PMTLD can be more effective and controllable. However, the preliminary researches were focusing on the characteristic analysis and only discussed its performance on a pendulum-type structure. More studies on the application for offshore engineering should be carried out.

In this paper, the two-dimensional fluid-structure interaction (FSI) problem of a floating platform equipped with PMTLD subjected to water wave loading is considered. The simulation needs numerical methods for both fluid and rigid body dynamics. The coupling algorithm has to satisfy the kinematic continuity (same displacement and velocity) and dynamic continuity (equilibrium of stresses) on the interface in between them. The nonlinear potential flow and two-phase Navier-Stokes models are employed for the hydrodynamic computation. The potential-flow model is solved by the inviscid Eulerian-Lagrangian (IEL) method, which involves a mixed-type boundary value problem solver implemented by BEM with linear element and the free-surface particle tracker via the second-order Tayler series expansion. Grilli et al. [32] studied the wave problem in a similar frame and successfully simulated the wave absorption behavior by setting an appropriate radiation condition. Grilli and Horrillo [33] verified the numerical method by a shoaling experiment. These studies didn't incorporate the rigid body dynamics in the wave field. To do so, the Newmark method with linear acceleration assumption is adopted in this paper. The common numerical instability issue arises due to incompatible solutions between fluid field and body motion. Sen [34] obtained the converged solutions of fluid field and body dynamics iteratively. Van Daalen [35] combined the governing equations of the body and fluid to derive an additional integral equation, which yields the compatible solution simultaneously. His method requires little extra computational effort but avoids numerical iterations. Tanizawa [36] provided a similar formula in the implicit algorithm. Hermans [37] calculated the reflection and transmission coefficients of a flexible platform in waves. Koo and Kim [38] used direct and indirect mode-decomposition methods and found the nonlinearity could make the second and third harmonic sway forces bigger than the first harmonic component. Jung et al. [39] carried out wave tank experiments to study the viscous effect on a freely rolling floating body. He concluded the linear potential theory underestimates the roll motion at lower frequencies because of the lack of eddy making damping. Kim et al. [40] studied the coupling effects between the ship and the sloshing tank above it. The nonlinearity that comes from the sloshing fluid could significantly affect the ship's stability. Guerber et al. [41] and Dombre et al. [42] distinguished the difference between several numerical schemes for simulating forced and free motion of a fully-submerged body. Many other strategies, such as mode decomposition method [43, 44] and indirect method [45], have been also proposed for solving potential

flow in FSI problems. In this paper, the strongly coupled algorithm is completed via iterative steps. The linear equivalent mechanical model is adopted for PMTLD exclusively. This mechanical model involves several sets of mass-spring-dashpot systems and has its dynamic characteristics the same as actual PMTLD. Therefore the fluid computation can be omitted and transferred into a simple calculation of motion equations. Besides, it is useful to design the PMTLD by analogy with TMD. The other two-phase Navier-Stokes model has been also studied in the paper. Compared to the potential flow model, it can describe the effect on structure more appropriately by including some realistic phenomena, such as viscous effect, vortex, and breaking waves. Piperno et al. [46] and Farhat and Lesoinne [47] showed the accuracy of the explicit scheme for Navier-Stokes flow. However, the explicit schemes have some stability issues, especially when the added mass effect is strong. The semi-implicit scheme was then proposed. It consists of an implicit solver for solid (usually the Neumann part affecting the stresses) and an explicit solver for the other part (usually the Dirichlet part affecting the fluid velocity) [48]. Matthies et al. [49] applied the implicit formulation to solve the FSI problem by the arbitrary Lagrangian-Eulerian (ALE) framework and his partitioned approach. Rodrigues et al. [50] applied FEM for the mooring lines of a floating drilling platform. Palm et al. [51] studied the motion of the wave energy converters by combining his VOF-RANS solver and FEM. Tezduyar [52] demonstrates the numerical results of some common topics in ocean engineering, such as propellers, pipes, free-surface flow, and sloshing phenomenon. Numerical approaches and their applications can be referred to textbooks [53]. In this paper, FEM is employed to spatially discretize the Navier-Stokes equations. VOF method and the level set equations [54, 55] are applied to solve the free surface motion. An immersed boundary method (IBM) [56] in conjunction with Nitsche's technique is introduced to complete the fluid-solid coupling. For PMTLD, the linear Darcy's flow and quadratic Forchheimer flow regimes are considered for the extra effect induced by the porous media. The fluid computation is implemented by the scientific toolkit Proteus [57] and the motion of the solid phase was simulated via Chrono's multibody dynamics engine [58]. Both Proteus and Chrono are open-source frameworks and available in the public domain.

This manuscript is organized as follows. Sections 2 and 3 provide details of the numerical methods used in the potential flow and two-phase Navier-Stokes flow models, respectively. Section 4 describes the numerical techniques for wave generation and absorption. Section 5 presents the design strategy for PMTLD. Section 6 presents the performance of PMTLD and compares the numerical method by several benchmark tests. The advantages of the PMTLD on offshore structure are briefly concluded in section 7.

2. NONLINEAR POTENTIAL FLOW

2.1. Governing equations and boundary conditions

The configuration of the rectangular PMTLD attached on a floating platform in the wave field is shown in Fig. 1. For the incompressible, inviscid, and irrotational fluid, the continuity and momentum equations of fluid can be expressed as:

$$\nabla \cdot \boldsymbol{u} = 0 \tag{1}$$

$$\rho \left[\frac{\partial \boldsymbol{u}}{\partial t} + (\boldsymbol{u} \cdot \nabla)\boldsymbol{u}\right] = -\nabla p + \nabla p_d + \rho \boldsymbol{g} \tag{2}$$

where ρ is the fluid density, $\boldsymbol{u}$ is the fluid velocity, p is the pressure, p_d is the pressure drop due to the porous media, and $\boldsymbol{g}$ is the gravitational acceleration. Note that in fresh water, $\nabla p_d = 0$, then the nonlinearity only comes from the convective term; when the porous media is involved, the Darcy's flow and Forchheimer flow regimes are considered, therefore the gradient of pressure drop can be expressed as [59]:

$$\nabla p_d = -\frac{\gamma \mu}{\kappa}(\boldsymbol{u} - \boldsymbol{v}) - \frac{\gamma c_F \rho}{\sqrt{\kappa}}|\boldsymbol{u} - \boldsymbol{v}|(\boldsymbol{u} - \boldsymbol{v}) \tag{3}$$

where $\boldsymbol{v}$ is the velocity of porous media, μ is the dynamic viscosity of fluid, γ and κ are the porosity and permeability of porous media, respectively, c_F is a dimensionless constant determined by experiments [60, 61]. Note that if $\boldsymbol{u}$ is sufficiently small, the first linear-damping term in the right-hand side of Eq. (3) dominates, while the second quadratic function becomes significant as $\boldsymbol{u}$ increases and the drag due to solid obstacles is comparable with the surface drag due to friction. In potential flow, the fluid velocity can be expressed by the gradient of the potential function ϕ as:

$$\boldsymbol{u} = \nabla \phi \tag{4}$$

Therefore the Laplace equation should be satisfied as:

$$\nabla^2 \phi = 0 \tag{5}$$

The kinematic boundary condition on the free surface $\Gamma_{f,c}$ and $\Gamma_{f,d}$ can be expressed as:

$$\frac{D\boldsymbol{R}}{Dt} = \boldsymbol{u} \tag{6}$$

where $\boldsymbol{R}$ is the location of a free-surface particle. For wave channel, the dynamic boundary condition on the free surface $\Gamma_{f,c}$ can be expressed as:

$$\frac{\partial \phi}{\partial t} + \frac{1}{2}|\nabla \phi|^2 + g\eta = 0 \tag{7}$$

where η is the wave elevation. For sloshing fluid, the dynamic boundary condition on the free surface $\Gamma_{f,d}$ can be expressed as:

$$\frac{\partial \phi}{\partial t} + \frac{1}{2}|\nabla \phi|^2 + (\phi - \psi)[\alpha_1 + \alpha_2|\nabla \phi - \nabla \psi|] + g\eta = 0 \tag{8}$$

where $\alpha_1 = \gamma \mu / \kappa \rho$ and $\alpha_2 = \gamma c_F / \sqrt{\kappa}$ are constants related to the nature of the porous media that can be determined by experiment, ψ is the velocity potential of the porous media. On the wetted boundaries $\Gamma_{w,c}$, $\Gamma_{b,c}$, $\Gamma_{w,d}$, $\Gamma_{b,d}$, and $\Gamma_{p,c}$, the impermeable condition is taken as:

$$\frac{\partial \phi}{\partial n} = \dot{x} \cdot n \tag{9}$$

where n denotes the normal vector pointing outward to the fluid boundary Γ, $\dot{x}$ is the velocity of the node on the wetted boundary. For the channel, the absorption of a wave of permanent form with velocity c can be represented by the radiation condition on absorption boundary $\Gamma_{r,c}$ as [32]:

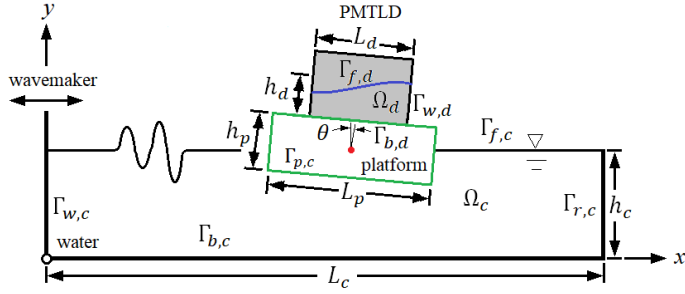$$\frac{\partial \phi}{\partial n} = -\frac{1}{c}\frac{\partial \phi}{\partial t} \tag{10}$$

FIGURE 1: THE CONFIGURATION OF THE RECTANGULAR PMTLD ATTACHED ON A FLOATING PLATFORM IN WAVE FIELD FOR POTENTIAL FLOW MODEL.

2.2. IEL method

By applying Green's second identity to Laplace's equation, the boundary integral equation (BIE) for a fluid boundary Γ can be obtained as:

$$c_p \phi_p = \int_{\Gamma} \left(\frac{\partial G}{\partial n} \phi - G \frac{\partial \phi}{\partial n} \right) d\Gamma \tag{11}$$

where G is the fundamental solution with source point p and c_p is the resulting flux. In this paper, the BIE is discretized and the integrals are implemented by BEM. Therefore Eq. (11) can be rewritten in matrix form as:

$$\mathbf{A}\{\phi\} = \mathbf{B}\{\phi_n\} \tag{12}$$

where $\mathbf{A}$ and $\mathbf{B}$ are the kernel matrices, $\{\phi\}$ and $\{\phi_n\}$ are the vectors containing the potential and the normal velocity at all of the boundary nodes, respectively. Eq. (12) arises a mixed-type BVP solved by giving ϕ on the free surface and ϕ_n [as shown in Eq. (9)] on the wetted boundaries. The free-surface particle is tracked via the second-order Taylor series expansion during a small time step Δt as:

$$R(t + \Delta t) = R(t) + \Delta t \frac{DR}{Dt} + \frac{\Delta t^2}{2}\frac{D^2 R}{Dt^2} + O[\Delta t^3] \tag{13}$$

$$\phi(t + \Delta t) = \phi(t) + \Delta t \frac{D\phi}{Dt} + \frac{\Delta t^2}{2}\frac{D^2 \phi}{Dt^2} + O[\Delta t^3] \tag{14}$$

The first-order derivative in Eq. (13) is obtained by the kinematic boundary condition, while the first-order derivative in Eq. (14) can be obtained by the Bernoulli equation for $\Gamma_{f,c}$ and $\Gamma_{f,d}$ as:

$$\frac{D\phi}{Dt} = -g\eta + \frac{1}{2}|\nabla \phi|^2 \tag{15}$$

$$\frac{D\phi}{Dt} = -g\eta + \frac{1}{2}|\nabla \phi|^2 - \alpha_1(\phi - \psi) - \alpha_2|\nabla\phi - \nabla\psi|(\phi - \psi) \tag{16}$$

The second-order derivatives of R and ϕ can be obtained as:

$$\frac{D^2 R_i}{Dt^2} = \frac{\partial^2 \phi}{\partial t \partial x_i} + u_j \frac{\partial^2 \phi}{\partial x_j \partial x_i} \quad ; i = 1,2 \ , j = 1,2 \tag{17}$$

$$\frac{D^2 \phi}{Dt^2} = u_i \frac{Du_i}{Dt} - g \frac{D\eta}{Dt} \quad ; i = 1,2 \tag{18}$$

A new unknown variable $\phi_t = \partial\phi/\partial t$ appears in Eqs. (17) and (18). Since ϕ_t also satisfies Laplace's equation, another mixed type BVP for ϕ_t and ϕ_{tn} arises and needs to be solved. The Dirichlet condition on the free surface $\Gamma_{f,c}$ and $\Gamma_{f,d}$ is given as:

$$\phi_t = \frac{D\phi}{Dt} - |\nabla\phi|^2 \tag{19}$$

The Neumann condition on the wetted boundaries $\Gamma_{w,c}$, $\Gamma_{b,c}$, $\Gamma_{w,d}$, $\Gamma_{b,d}$, and $\Gamma_{p,c}$ is given as:

$$\phi_{tn} = \ddot{x} \cdot n - (u \cdot \nabla)\phi_n \tag{20}$$

The Neumann condition on the absorption boundary $\Gamma_{r,c}$ is given as:

$$\phi_{tn} = c\frac{\partial^2 \phi}{\partial s^2} \tag{21}$$

where $\ddot{x}$ is the acceleration of the node on the wetted boundary, s denotes the unit tangential vector of the boundary. Fortunately, the domain geometry remains unchanged at the current time step so $\mathbf{A}$ and $\mathbf{B}$ shown in Eq. (12) can be reused. Therefore the free-surface tracker is solved very fast.

2.3. Dynamics of floating body and FSI coupling

The floating platform has three degrees of freedom (namely free to sway, heave, and roll). The motion equation can be expressed as:

$$M_b \ddot{x}_G = F + M_b g \tag{22}$$

$$I_G \ddot{\theta}_G = M \tag{23}$$

where $\ddot{x}_G$ and $\ddot{\theta}_G$ are the translational and angular accelerations of the body center of mass, respectively, M_b and I_G are the mass and moment of inertia of the body, respectively. The resultant force F and moment M from PMTLD and waves can be expressed as:

$$F = \int_{\Gamma_{p,c}} pn \ d\Gamma + \int_{\Gamma_{w,d}+\Gamma_{b,d}} pn \ d\Gamma \tag{24}$$

$$M = \int_{\Gamma_{p,c}} p(r \times n) \ d\Gamma + \int_{\Gamma_{w,d}+\Gamma_{b,d}} p(r \times n) \ d\Gamma \tag{25}$$

where r is the position of a point on the body boundary with respect to the center of mass, and the pressure along the wetted boundary $\Gamma_{p,c}$, $\Gamma_{w,d}$ and $\Gamma_{b,d}$ can be obtained by the Bernoulli equation:

$$p = -\rho\left(\frac{\partial\phi}{\partial t} + \frac{1}{2}|\nabla\phi|^2 + g\eta\right) \tag{26}$$

The Newmark method based on constant acceleration assumption is employed to solve the motion equation as:

$$\ddot{x}_{G,k+1} = \frac{F_{k+1}}{M_b} \tag{27}$$
$$\dot{x}_{G,k+1} = \dot{x}_{G,k} + 0.5\Delta t(\ddot{x}_{G,k} + \ddot{x}_{G,k+1}) \tag{28}$$
$$x_{G,k+1} = x_{G,k} + \Delta t\dot{x}_{G,k} + 0.25\Delta t^2(\ddot{x}_{G,k} + \ddot{x}_{G,k+1}) \tag{29}$$

where k is the time step. This scheme is unconditionally stable. Besides, no sub-step is required. The resultant force used in Newmark scheme comes from the fluid field. It is not a priori known because, to solve the fluid field, the body kinematics used in Eqs. (9) and (20) should be given but they depend on body motion as:

$$\dot{x} = (\dot{x}_G + \dot{\theta}_G \times r)\cdot n \tag{30}$$
$$\ddot{x} = [\ddot{x}_G + \dot{\theta}_G \times r + \dot{\theta}_G \times (\dot{\theta}_G \times r)]\cdot n \tag{31}$$

To solve the fluid field and body motion simultaneously, the iterative algorithm illustrated in Algorithm 1 is used [42].

Algorithm 1: Algorithm of the potential-flow model for wave-structure interactions.
do $k > 0$
Start iterative step with the solution at k_{th} time step as an initial guess
$\epsilon = abs(\ddot{x}_{G,k,i} - \ddot{x}_{G,k,i-1})$
   do while $\epsilon > \epsilon_{tolerance}$
      Solve ϕ_i and $\phi_{n,i}$ (the first BVP)
      Solve $\phi_{t,i}$ and $\phi_{tn,i}$ (the second BVP)
      Calculate pressure along wetted boundaries
      Calculate force and moment act on the floating body
      Define predictor of force and moment:
            $F^* = F_{k,i} + \omega(F_{i-1}^* - F_{k,i})$
      Solve rigid body motion (Newmark method)
      Update free surface and body boundary $S_{k,i+1}$ and
      $\phi_{k,i+1}$
   end do
$x_{k+1} = x_{k,i+1}$
$\dot{x}_{k+1} = \dot{x}_{k,i+1}$
$\ddot{x}_{k+1} = \ddot{x}_{k,i+1}$
$\phi_{k+1} = \phi_{k,i+1}$
$S_{k+1} = S_{k,i+1}$
end do

2.4. Equivalent mechanical model
For the rectangular PMTLD shown in Fig. 2, the corresponding equivalent mechanical model consists of a fixed mass m_f located at the heights Z_f, and an infinite mass-dashpot-spring systems (denoted by m_n, c_n, and k_n) located at the heights Z_n as shown in Fig. 3. This model can be dynamically equal to the linear PMTLD in terms of resultant force, overturning moment, and kinetic energy. The equivalent masses, stiffness k_n, damping ratios ξ_n, location heights, can be expressed as [29]:

$$m_n = \frac{8\gamma\rho B}{a_n^3 L_d}tanha_n h_d \tag{32}$$
$$k_n = m_n\omega_n^2 = \frac{8\gamma\rho gB}{a_n^2 L_d}tanh^2 a_n h_d \tag{33}$$
$$\xi_n = \frac{\alpha_1}{2\omega_n} = \frac{\gamma\mu}{2\kappa\rho\omega_n} = \frac{\gamma\mu}{2\kappa\rho}\sqrt{\frac{cotha_n h_d}{a_n g}} \tag{34}$$
$$Z_n = h_d + \frac{2}{a_n sinha_n h_d} - \frac{1}{a_n tanha_n h_d} \tag{35}$$
$$m_f = m_w - \sum_{n=0}^{\infty} m_n = \gamma\rho BL_d h_d\Big[1 - \sum_{n=0}^{\infty}\frac{8}{a_n^3 L_d^2 h_d}tanha_n h_d\Big] \tag{36}$$
$$Z_f = \frac{1}{m_f}\Big[\gamma\rho B\Big(\frac{L_d h_d^2}{2} + \frac{L_d^3}{12}\Big) - \sum_{n=0}^{\infty} m_n Z_n\Big] \tag{37}$$

where $a_n = (2n+1)\pi/L_d$, $n = 0,1,2...$, $m_w = \gamma\rho L_d B h_d$ denotes the total water mass in the tank. The wave elevation on the right-side wall can be expressed in terms of the equivalent displacement x_n as:

$$\eta = \sum_{n=0}^{\infty}\frac{4}{a_n L_d}tanha_n h_d \cdot x_n \tag{38}$$

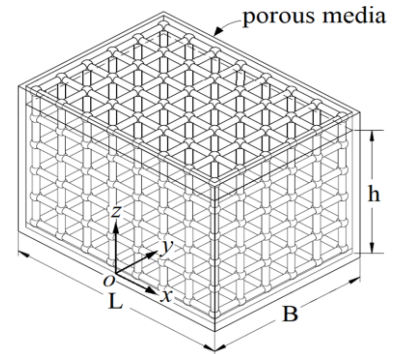In the equivalent model, the response of the PMTLD can be solved by the state space method [62].

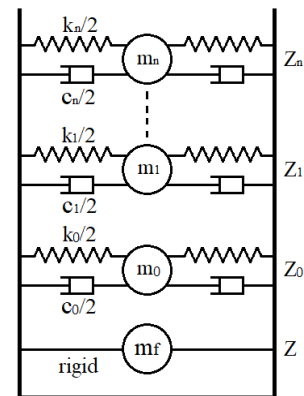**FIGURE 2**: THE SCHEMATIC DIAGRAM OF THE POROUS MEDIA IN A RECTANGULAR TANK.

FIGURE 3: THE SCHEMATIC DIAGRAM OF THE EQUIVALENT MECHANICAL MODEL.

3. TWO-PHASE NAVIER-STOKES FLOW

3.1. Governing equations
The configuration of the FSI problem in two-phase Navier-Stokes flow is shown in Fig. 4. The entire fluid

domain consists of two incompressible Newtonian phases, air and water, separated by a sharp material interface. Across the interface, the density and viscosity are discontinuous but velocity and pressure are continuous. Surface tension is neglected. The continuity and Navier-Stokes equations formulated for each fluid phase are:

$$\nabla \cdot \boldsymbol{u}_i = 0 \tag{39}$$

$$\rho \left[\frac{\partial \boldsymbol{u}_i}{\partial t} + (\boldsymbol{u}_i \cdot \nabla)\boldsymbol{u}_i\right] = -\nabla p_i + \nabla \cdot \boldsymbol{\sigma}_i + \boldsymbol{f} \tag{40}$$

where $i \in \{w, a\}$, $\boldsymbol{\sigma}_i$ is the stress tensor, $\boldsymbol{f}$ is the body force, and subscript w and a denotes the water and air phases, respectively. The proper boundary conditions on the air-water interface are provided based on the assumption of continuity of velocity and stress across the interface Γ_f as:

$$p_w = p_a, \ \boldsymbol{u}_w = \boldsymbol{u}_a, \ \boldsymbol{\sigma}_w \cdot \boldsymbol{n} = \boldsymbol{\sigma}_a \cdot \boldsymbol{n} \tag{41}$$
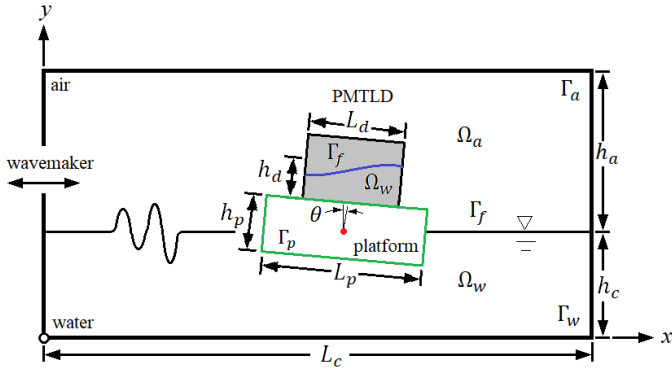

FIGURE 4: THE CONFIGURATION OF THE RECTANGULAR PMTLD ATTACHED ON A FLOATING PLATFORM IN WAVE FIELD FOR TWO-PHASE NAVIER-STOKES MODEL.

3.2. LS method

By using Eq. (41) and neglecting the loss of smoothness due to the jump discontinuities in density and viscosity, the continuous global pressure and velocity fields can be introduced. Therefore the single Navier-Stokes equations for the entire fluid domain can be obtained as:

$$\nabla \cdot \boldsymbol{u} = 0 \tag{42}$$

$$\rho \left[\frac{\partial \boldsymbol{u}}{\partial t} + (\boldsymbol{u} \cdot \nabla)\boldsymbol{u}\right] = -\nabla p + \nabla \cdot (2\mu\boldsymbol{\epsilon}) + \boldsymbol{f} \tag{43}$$

where $\boldsymbol{\epsilon} = \frac{1}{2}(\nabla \boldsymbol{u} + \nabla \boldsymbol{u}^T)$. The density and viscosity of the two-fluid system are given by:

$$\rho = \rho_w H(\psi) + \rho_a[1 - H(\psi)] \tag{44}$$

$$\mu = \mu_w H(\psi) + \mu_a[1 - H(\psi)] \tag{45}$$

where $H(\psi)$ is the Heaviside function expressed as:

$$H(\psi) = \begin{cases} 0 & , \psi < 0 \\ 1/2 & , \psi = 0 \\ 1 & , \psi > 0 \end{cases} \tag{46}$$

Note that Eq. (42) equals Eq. (1) but it is used in Ω_a and Ω_w.

In this paper, the level set method is used to distinguish the fluid subdomains. The free surface is defined by the level set function $\psi = 0$, and $\psi > 0$ for the water phase, $\psi < 0$ for the air phase. The free surface evolution can be described by the level set equation as:

$$\frac{\partial \psi}{\partial t} + \boldsymbol{u} \cdot \nabla \psi = 0 \tag{47}$$

To avoid unacceptable mass conservation errors, the differential form of the mass conservation equation yields the volume fraction equation that can be written as:

$$\frac{\partial \alpha}{\partial t} + \nabla \cdot (\alpha \boldsymbol{u}) = 0 \tag{48}$$

where α is the volume fraction. Eqs. (42)~(47) constitute a complete model of the two-phase flow at the continuous level. The Eikonal equation is added for calculation of a signed distance function ψ_d as:

$$|\nabla \psi_d| = 1 \ \text{and} \ \psi_d = 0 \ \text{on} \ \Gamma_f \tag{49}$$

The volume fraction is linked to the signed distance function by:

$$\lambda \Delta \psi' = H(\psi_d + \psi') - \alpha \ \text{with} \ \nabla \psi' \cdot \boldsymbol{n} = 0 \tag{50}$$

where λ is a parameter that penalizes the deviation of ψ' from a global constant.

3.3. FSI coupling via force-displacement co-simulation

For space discretization, the residual-based variational multiscale (RBVMS) method [63] is applied to Eqs. (42), (43), and (47)~(50) with linear triangular mesh. Some strategies for improving stability and accuracy are employed but not addressed in this paper for simplicity [64]. The Nitsche's technique and an IBM are used to accommodate the solid motion [65], and then the motion of the solid-phase was calculated via Chrono's multibody dynamics engine [58]. After conducting the solid solver, the rigid body's position and velocity are reported to the fluid solver to provide boundary conditions. The numerical process is illustrated in Algorithm 2.

Algorithm 2: Algorithm of the two-phase Navier-Stokes model for wave-structure interactions.

do $k > 0$
    Discretize and solve Navier-Stokers equations
    Advance the level set and volume fraction
    Re-initialize the level set function (Eikonal equation)
    Apply mass conservative correction
    Update level set function and volume fraction
    Calculate pressure and force
    Solve rigid body motion (Chrono)
end do

4. WAVE GENERATION AND WAVE ABSORPTION

In our examples, the periodic waves are generated by the piston wavemaker. For the potential flow model, the

© 2022 by ASME

estimation of the relation between the target wave height H_0 and the demand stroke of wavemaker S is described as [66]:

$$\frac{H_0}{S} = \frac{2(cosh 2k_0 h_c - 1)}{sinh 2k_0 h_c + 2k_0 h_c} \tag{51}$$

where k_0 is the wavenumber. Therefore the harmonic displacement of the wavemaker is given by:

$$x_f = \frac{S}{2} sin(\omega_f t) \tag{52}$$

The wavemaker's displacement changes the geometry of the fluid domain. Meanwhile the first- and second-order time derivatives of Eq. (52) (i.e. the velocity and acceleration of the piston wavemaker) will be used in Eqs. (9) and (20). For the outlet of the channel, the radiation condition shown in Eq. (10) is applied. For the two-phase Navier-Stokes model, the relaxation zones have been set for wave generation and wave absorption as shown in Fig. 5. In the generation zone, this method does not need to move the physical boundary of the wavemaker to generate waves but gradually impose the target wave kinematics, such as velocity and free surface position. In the absorption zone, it does not use the radiation boundary condition but imposes a target velocity of zero. The target velocity is given by adding a source term in the Navier-Stokes equations as [67]:

$$\rho \left(\frac{\partial \boldsymbol{u}}{\partial t} + \boldsymbol{u} \cdot \nabla \boldsymbol{u} - \boldsymbol{g} \right) - \nabla \cdot \boldsymbol{\sigma} = \alpha_b \alpha_c (\boldsymbol{u} - \boldsymbol{u}_t) \tag{53}$$

where α_b is a blending function, α_c is a constant, and $\boldsymbol{u}_t$ is the target velocity. The blending function α_b is given by:

$$\alpha_b = \frac{e^{d^{3.5}} - 1}{e - 1} \tag{54}$$

where d is the normalized scaled distance from the boundary to the end of the relaxation zone. $d = 1$ means the source term is fully imposed at the boundary and $d = 0$ means the source term vanishes at the end of the relaxation zone.
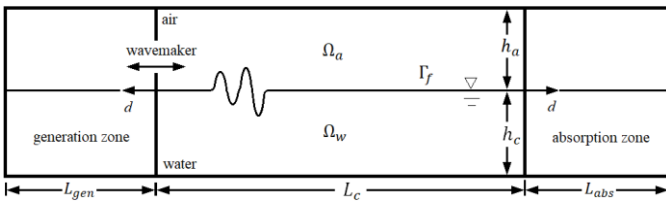

FIGURE 5: ILLUSTRATION OF RELAXATION ZONES AND THE SCALED DISTANCE IN THE NUMERICAL CHANNEL.

5. DESIGN PARAMETERS OF PMTLD

Consider only the first modal response of the PMTLD, it can be designed based on the analogy with TMD [27]. Therefore the tuning frequency ratio f_t and optimal damping ratio ξ_{opt} can be obtained by [68]:

$$f_t = \frac{\omega_0}{\omega_s} = \frac{1}{1 + R_m} \tag{55}$$

$$\xi_{opt} = \sqrt{\frac{3 R_m}{8(1 + R_m)}} \tag{56}$$

where ω_s is the natural frequency of the main structure, and $R_m = \frac{m_0}{m_f + M_b}$ is the mass ratio. Note that Eqs. (55) and (56) are derived based on some simple assumptions, so the design parameters may not be truly 'optimal' in our case. However, they are still close and useful. The optimal parameters for different configurations of mass dampers can be referred to textbooks [69]. Once R_m is given by the designer, the natural frequency and the damping ratio of PMTLD can be calculated. The corresponding tank dimensions and porous media property can be determined. A simple design chart is shown in Fig. 6.
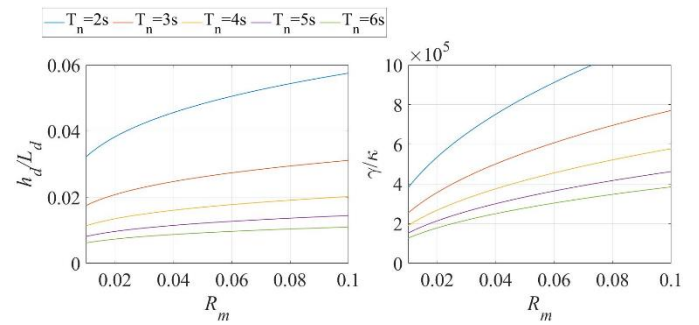

FIGURE 6: DESIGN CHART OF TANK DIMENSIONS AND POROUS MEDIA PROPERTY FOR DIFFERENT MASS RATIOS.

6. EXAMPLES

6.1. Dynamic characteristics of floating platform

A free-decay test is carried out to characterize the floating body dynamics. Consider the two-dimensional FSI problem has unit width. The channel has its length = 10 m and water depth = 2 m. The rectangular platform has its length = 1 m, height = 0.5 m, and density = 450 kg/m³, resulting the mass = 225 kg and moment of inertia = 23.44 kg-m². No waves are applied to the flow field. The rectangular platform is not equipped with PMTLD. Its center of gravity is placed at the height of the still water surface and has an initial inclined angle $\theta_0 = 5°$ and $\theta_0 = 10°$. The schematic diagram of element and node distribution on the computational domains and boundaries of the wave channel and floating body are shown in Fig. 7. For BEM used in the potential flow model, 1714 two-node linear elements are distributed on the wave boundary. For FEM used in the NS flow model, 375k triangular cells are distributed in the entire domain.
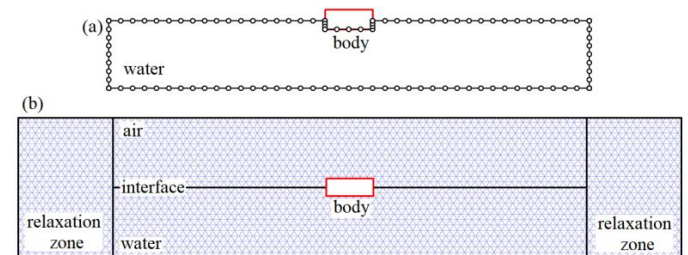

FIGURE 7: THE ELEMENT AND NODE DISTRIBUTION ON THE COMPUTATIONAL DOMAINS AND

The free-vibration responses of the floating platform when $\theta_0 = 5°$ by two numerical models are shown in Fig. 8. The corresponding response spectra are shown in Fig. 9. For sway motion, the drifts in both models are small, while the harmonics can be observed in the time histories of velocity and acceleration. Since the horizontal force comes from the pressure difference between the left and right sides of the body, which is in sync with the roll motion. This phenomenon explains the sway and roll motions have the same oscillatory frequency of 0.6104 Hz as shown in Fig. 9. For the heave motion, both models show similar oscillation due to the changing buoyancy in the vertical direction. The heaving frequency = 0.6714 Hz as shown in Fig. 9. For the roll motion, the amplitude decay can be observed in the NS model since the viscous effect was considered. As it had been mentioned in the past research [39], wave damping is important to roll motion. Therefore the potential model may overestimate the rolling amplitude if no artificial wave damping is applied. However, they still give the same rolling frequencies shown in Fig. 9. The free-vibration responses of the floating platform when $\theta_0 = 10°$ by two numerical models are shown in Fig. 10. The corresponding response spectra are shown in Fig. 11. A larger initial condition does not significantly change the dynamic characteristics of the floating body. However, the difference between the two numerical models may grow because their different physical assumptions in wave field will affect the FSI simulation.
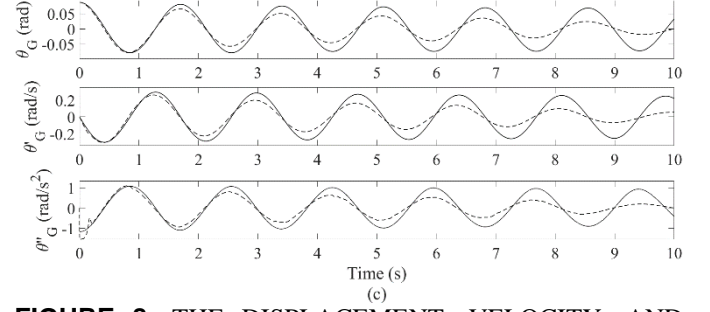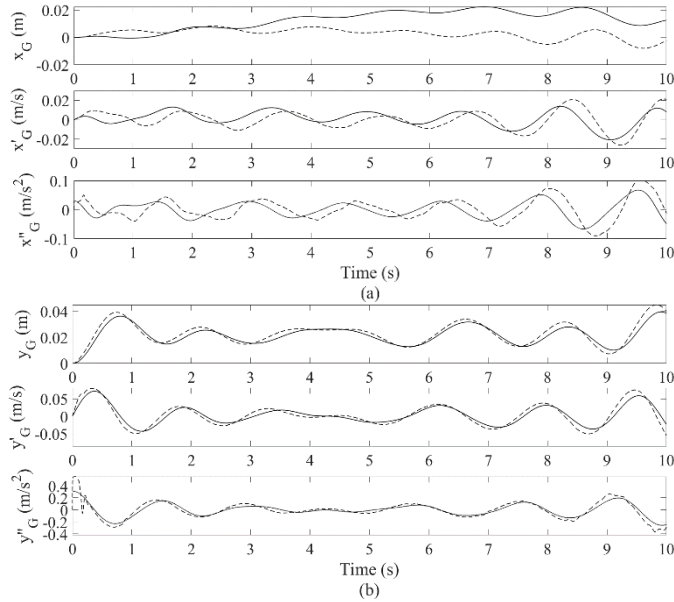

FIGURE 8: THE DISPLACEMENT, VELOCITY, AND ACCELERATION OF A FREELY MOVING FLOATING PLATFORM WHEN $\theta_0 = 5°$ (A) SWAY, (B) HEAVE, (C) ROLL (SOLID LINE: POTENTIAL FLOW, DASHED LINE: NS FLOW).
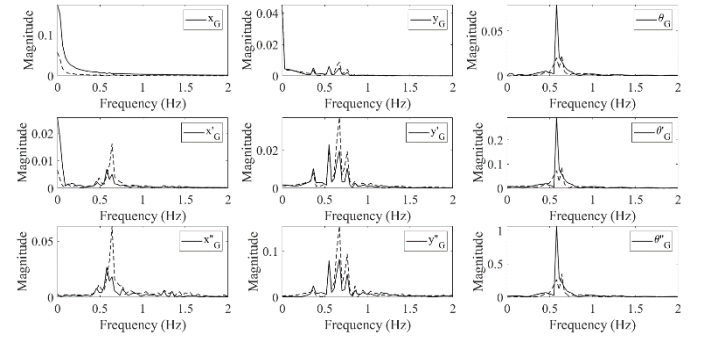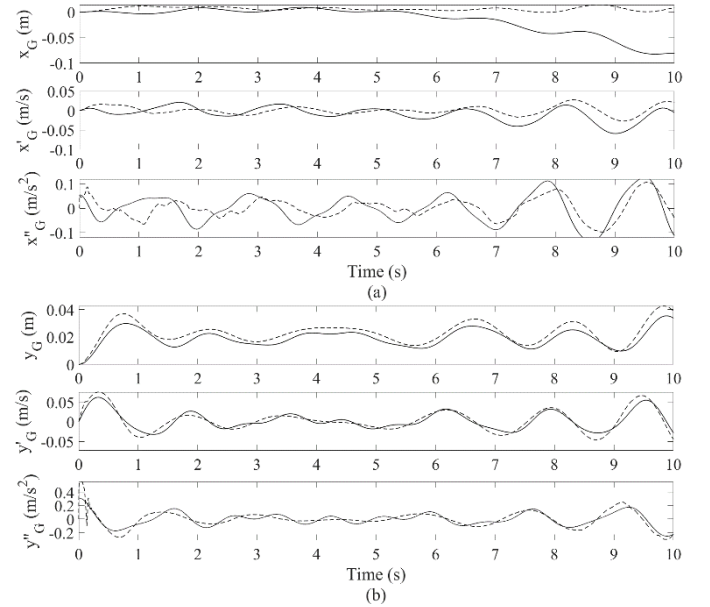

FIGURE 9: THE RESPONSE SPECTRA OF FREE VIBRATION OF THE FLOATING PLATFORM WHEN $\theta_0 = 5°$ (SOLID LINE: POTENTIAL FLOW, DASHED LINE: NS FLOW).

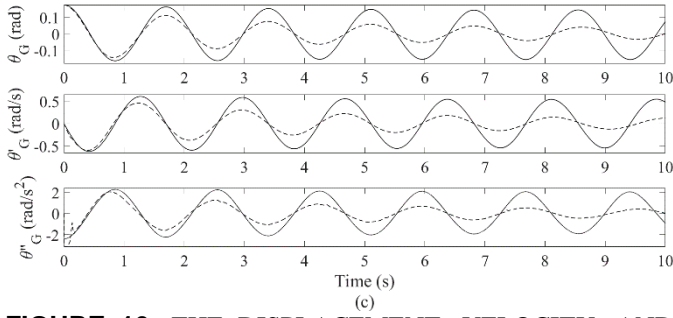**FIGURE 10**: THE DISPLACEMENT, VELOCITY, AND ACCELERATION OF A FREELY MOVING FLOATING PLATFORM WHEN $\theta_0 = 10°$: (A) SWAY, (B) HEAVE, (C) ROLL (SOLID LINE: POTENTIAL FLOW, DASHED LINE: NS FLOW).
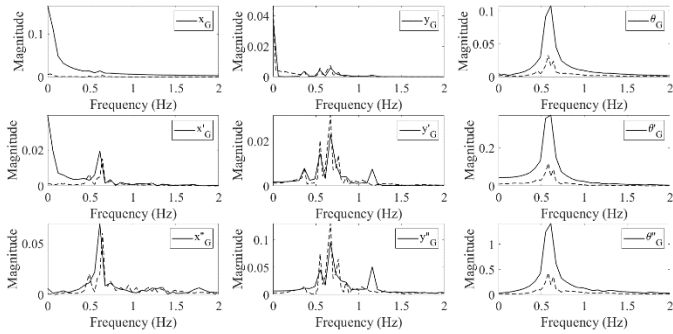

FIGURE 11: THE RESPONSE SPECTRA OF FREE VIBRATION OF THE FLOATING PLATFORM WHEN $\theta_0 = 10°$ (SOLID LINE: POTENTIAL FLOW, DASHED LINE: NS FLOW).

6.2. PMTLD on floating platform in waves

In this example, R_m is given as 0.1. When PMTLD is designed for the rolling mitigation ($\omega_s = 3.84$ rad/s), the tuning frequency can be obtained as 3.49 rad/s. Therefore the PMTLD has its length = 0.62 m and water depth = 0.049 m. The porosity of the porous media = 0.96. The optimal damping ratio = 18.4%, resulting $\alpha_1 = 1.28$ s^{-1} used in the numerical computation. α_2 is assumed to be a reasonable value as 5.0 m^{-1} for convenience [30]. The masses of the tank and porous media are neglected. The harmonic waves are generated to propagate along the x-direction, from left to right, with wave height = 0.05 m. In the two-phase NS model, the lengths of the wave generation and absorption zones are 2 m. The schematic diagrams of element and node distribution on the computational domains and boundaries of PMTLD are shown in Fig. 12. For BEM used in the potential flow model, 80 two-node linear elements are distributed on the PMTLD boundary. For FEM used in the NS flow model, 1211 triangular cells are distributed in the PMTLD domain. For the equivalent mechanical model, only the first modal moving mass is considered and the high-order modal moving masses are neglected for simplicity.
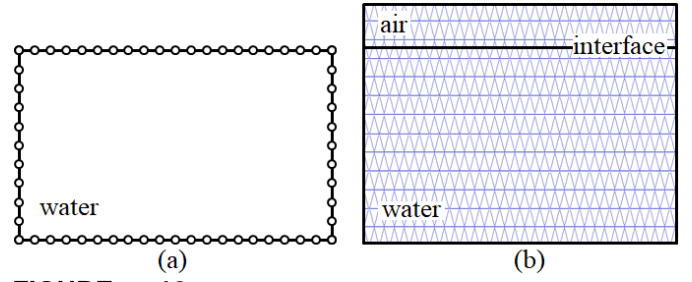

FIGURE 12: THE ELEMENT AND NODE DISTRIBUTION ON THE COMPUTATIONAL DOMAINS AND BOUNDARIES OF PMTLD (NOT TO SCALE): (A) POTENTIAL FLOW MODEL, (B) TWO-PHASE NS MODEL.

The forcing frequency ratio β is defined as the ratio between the frequency of the wavemaker's movement and the natural rolling frequency of the body. For the resonant case ($\beta = 1.0$), the sway, heave, and roll motions of the floating platform with and without PMTLD are shown in Figs. 13~15, respectively. For sway motion, PMTLD seems can slow down the lateral drift but will not be able to reduce the velocity and acceleration of the platform. For heave motion, the mean value of displacement is different as the PMTLD is installed because the additional weight of the water tank will change its static displacement. The oscillatory amplitudes are still the same shows that PMTLD is not effective for heaving reduction. For roll motion, a significant reduction can be observed. In the potential flow model, the PMTLD can cut down the rolling amplitude from $12°$ to $2.5°$ (80% of vibration), while in the NS flow model, the rolling amplitude decreases from $7.7°$ to $2.5°$ (67% of vibration). Considering the viscous effect from waves in the uncontrolled cases, the reduction ratio of 67% is a more reasonable value for reference. Although the potential flow model neglects the viscous effect, it still gives the same rolling amplitude as the NS model when PMTLD is applied. This shows the damping that comes from the porous media is more significant than that of the ambient waves. Therefore PMTLD provides an important resource in rolling mitigation. In our example, the results from the equivalent mechanical model and nonlinear potential flow model are very close. This implies the first modal response and the linear damping term dominate in PMTLD analysis.
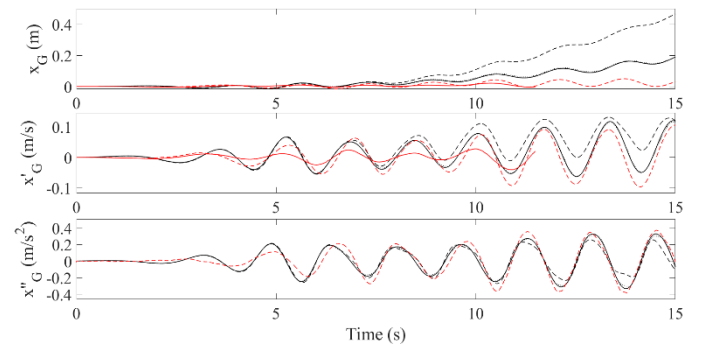

FIGURE 13: THE SWAY MOTIONS OF THE FLOATING PLATFORM WITH AND WITHOUT PMTLD WHEN $\beta = 1.0$ (BLACK SOLID LINE: POTENTIAL FLOW W/ PMTLD, BLACK DOTTED LINE: MECHANICAL MODEL

FIGURE 14: THE HEAVE MOTIONS OF THE FLOATING PLATFORM WITH AND WITHOUT PMTLD WHEN $\beta = 1.0$ (BLACK SOLID LINE: POTENTIAL FLOW W/ PMTLD, BLACK DOTTED LINE: MECHANICAL MODEL W/ PMTLD, BLACK DASHED LINE: POTENTIAL FLOW W/O PMTLD, RED SOLID LINE: NS FLOW W/ PMTLD, RED DASHED LINE: NS FLOW W/O PMTLD).
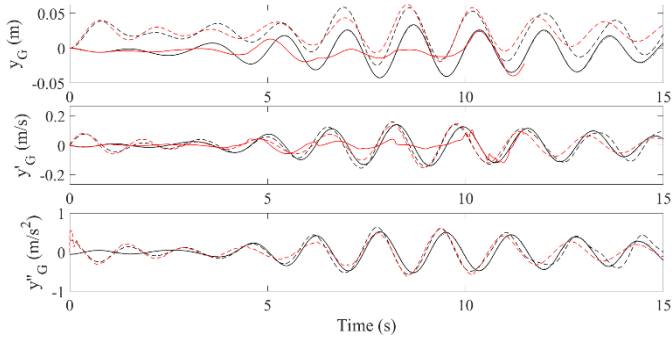

FIGURE 15: THE ROLL MOTIONS OF THE FLOATING PLATFORM WITH AND WITHOUT PMTLD WHEN $\beta = 1.0$ (BLACK SOLID LINE: POTENTIAL FLOW W/ PMTLD, BLACK DOTTED LINE: MECHANICAL MODEL W/ PMTLD, BLACK DASHED LINE: POTENTIAL FLOW W/O PMTLD, RED SOLID LINE: NS FLOW W/ PMTLD, RED DASHED LINE: NS FLOW W/O PMTLD).
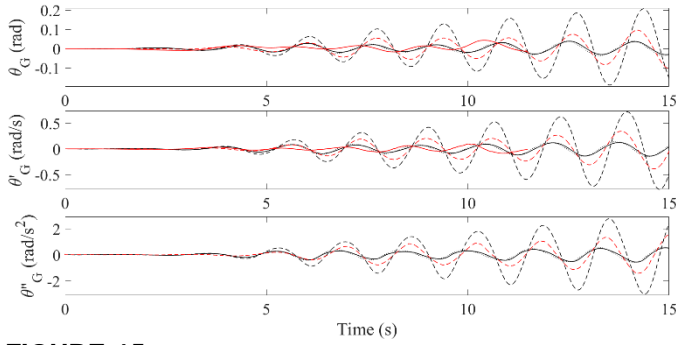
Fig. 16 shows the forces and moment act on the floating platform obtained from the potential flow model. For the horizontal force F_x, PMTLD produces the sloshing force that is out of phase with the wave load, but it is too small compared to the wave loading so it can not contribute to sway reduction. However, in our case, the effectiveness cannot be proved through the observation of the lateral drift since the sway motion does not subject to any constraint (such as mooring lines). For the vertical force F_y, the sloshing force is simply a dead load. PMTLD will not be effective for the heaving reduction as shown in Fig. 14. For the overturning moment M_θ, although the PMTLD is not perfectly tuned (or it will show a $180°$ phase lag between sloshing and wave moments), the sloshing moment can cancel out the wave-induced moment. Therefore PMTLD is effective for roll reduction. The parametric study and tuning condition for better performance of the PMTLD will be studied in the future.
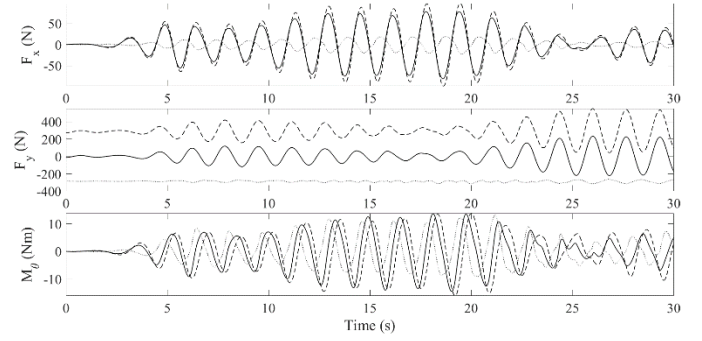

FIGURE 16: THE FORCES AND MOMENT ACT ON THE FLOATING PLATFORM WHEN $\beta = 1.0$ (SOLID LINE: TOTAL RESULTANT, DASHED LINE: WAVE LOAD, DOTTED LINE: PMTLD REACTION).

The frequency responses of the root mean squares (RMS) of the floating platform's roll motion are shown in Fig. 17. In the uncontrolled cases, resonance occurs at $\beta = 1$. The magnitudes of potential and NS models are different due to wave viscosity. As PMTLD is installed, the peaks of the response are shifted to $\beta = 1.05$. This implies the system's natural frequency has changed. The magnitudes of both models are close because the damping from porous media dominates. The overall reduction of the RMS response by PMTLD is about 70~80%.
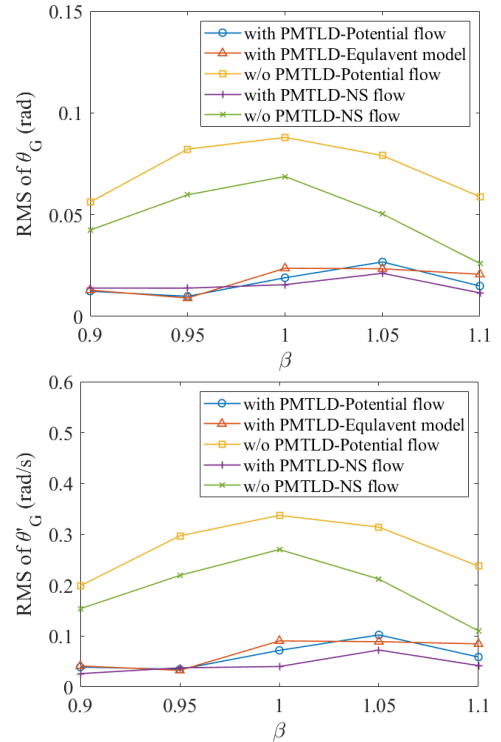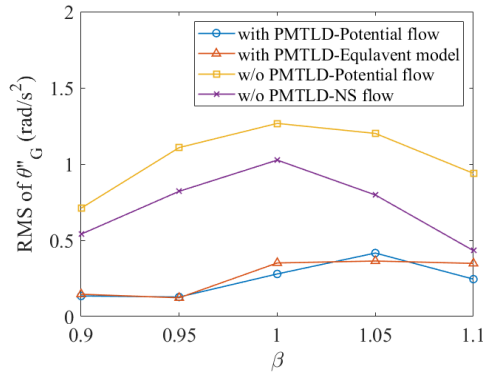
FIGURE 17: THE FREQUENCY RESPONSES OF THE FLOATING PLATFORM'S ROLL MOTION.

Table 1 shows the computational cost of three numerical models for a 10-second simulation. The computations were completed on the HPC machine QB3 at Louisiana Optical Network Infrastructure (LONI). Parallel computing is applied in three numerical schemes. Due to the simplicity of the spatial discretization and time-marching schemes of BEM, the potential-based method costs 9% of the computing time of the two-phase NS model. The equivalent mechanical model avoids the fluid computation for PMTLD so it cost the least.

TABLE 1: THE COMPUTATIONAL COST OF THREE NUMERICAL MODELS FOR A 10-SECOND SIMULATION.

	Equivalent model	Potential flow	NS flow
Number of core	16	16	48
CPU time (hr)	2.7	3	32

7. CONCLUSIONS

This paper presents the FSI simulation of a PMTLD on a floating platform in waves through the numerical methods that couple fluid computation and rigid-body dynamics for potential flow and two-phase Navier-Stokes flow models. The NS model describes the rolling oscillation better because it considers the damping of ambient waves. However, the viscous-induced damping is not significant compared to the energy dissipated by porous media. Therefore the numerical results of the controlled cases in both models are similar. Besides, the linear equivalent mechanical model also gives the same results in the controlled cases. This implies the first modal response and the linear damping term dominate in PMTLD analysis. PMTLD is effective for roll motion mitigation. At our resonance test, 67% of vibration can be reduced. The overall reduction of RMS response can be up to 80%. However, it does not produce a useful control force in the vertical direction so it is not validated for heaving control. Although the horizontal control force cancels out the wave loads, no obvious reduction in sway motion is observed since the horizontal drift is unconstrained. The PMTLD can be applied to moored floating bodies and wind turbine platforms for further investigation. Detail parametric studies on the tuning condition and optimal damping of PMTLD will be carried out in the future.

ACKNOWLEDGMENT

REFERENCE

[1] W. Burger, A.G. Corbet, Ship Stabilizers: A Handbook for Merchant Navy Officers. Chapter III - Anti-Rolling Devices in General (1966) 31-37.

[2] Y.H. Chen, C.H. Ko, Active tuned liquid column damper with propellers, Earthquake Engineering & Structural Dynamics. 32 (2003) 1627-1638.

[3] S.K. Yalla, A. Kareem, J.C. Kantor, Semi-active tuned liquid column dampers for vibration control of structures. Engineering Structures 23(2001) 1469-1479.

[4] O.A. Marzouk, A.H. Nayfeh, Control of ship roll using passive and active anti-roll tanks. Ocean Engineering 36 (2009) 661-671.

[5] V. Gattulli, R. Ghanem, Adaptive control of flow-induced oscillations including vortex effects, International Journal of Non-Linear Mechanics 34(5) (1999) 853-868.

[6] K. Kawano, Active control effects on dynamic response of offshore structures, Proceedings of the 3rd International Offshore and Polar Engineering Conference (1993) 594-598.

[7] H.H. Lee, S.H. Wong, R.S. Lee, Response mitigation on the offshore floating platform system with tuned liquid column damper, Ocean Engineering 33(8-9) (2006) 1118-1142.

[8] E.A. Bossanyi, The design of closed loop controllers for wind turbines, Wind Energy 3 (2000) 149-163.

[9] P.B. Andersen, L. Henriksen, M. Gaunaa, C. Bak, T. Buhl, Deformable trailing edge flaps for modern megawatt wind turbine controllers using strain gauge sensors, Wind Energy 13 (2010) 193-206.

[10] D. Castaignet, T.K. Barlas, T. Buhl, N.K. Poulsen, J.J. Wedel-Heinen, N.A. Olesen, C. Bak, T. Kim, Full-scale test of trailing edge flaps on a Vestas V27 wind turbine: Active load reduction and system identification, Wind Energy 17 (2013) 549-564.

[11] M. Rahman, Z.C. Ong, W.T. Chong, S. Julai, S.Y. Khoo, Performance enhancement of wind turbine systems with vibration control: A review, Renewable and Sustainable Energy Reviews 51 (2015) 43-54.

[12] G. Stewart, M. Lackner, Offshore wind turbine load reduction employing optimal passive tuned mass damping systems, IEEE Transactions on Control Systems Technology 21 (2013) 1090-1104.

[13] Y. Si, H.R. Karimi, H. Gao, Modelling and optimization of a passive structural control design for a spar-type floating wind turbine, Engineering Structure 69 (2014) 168-182.

[14] V.N. Dinh, B. Basu, Passive control of floating offshore wind turbine nacelle and spar vibrations by multiple tuned mass dampers, Structural Control and Health Monitoring 22 (2014) 152-176.

[15] S. Colwell, B. Basu, Tuned liquid column dampers in offshore wind turbines for structural control, Engineering Structure 31 (2009) 358-368.

[16] X. Tong, X. Zhao, A. Karcanias, Passive vibration control of an offshore floating hydrostatic wind turbine model, Wind Energy 21 (2018) 697-714.

[17] J. Chen, G. Zhan, Y. Zhao, Application of spherical tuned liquid damper in vibration control of wind turbine due to earthquake excitations, The Structural Design of Tall and Special Buildings 25 (2016) 431-443.

[18] P. Martynowicz, Vibration control of wind turbine tower-nacelle model with magnetorheological tuned vibration absorber, Journal of Vibration and Control 23 (2015) 3468-3489.

[19] P. Martynowicz, Control of a magnetorheological tuned vibration absorber for wind turbine application utilising the refined force tracking algorithm, Journal of Low Frequency Noise, Vibration and Active Control 36 (2017) 339-353.

[20] A. Staino, B. Basu, S. Nielsen, Actuator control of edgewise vibrations in wind turbine blades, Journal of Sound and Vibration 331 (2012) 1233-1256.

[21] Y.H. Chen, W.S. Hwang, W.H. Tsao, Nonlinear dynamic characteristics of rectangular and cylindrical TLD's, Journal of Engineering Mechanics 144 (2018) 06018004.

[22] S.M. Zahrai, S. Abbasi, B. Samali, Z. Vrcelj, Experimental investigation of utilizing TLD with baffles in a scaled down 5-story benchmark building, Journal of Fluids and Structures 28 (2012) 194-210.

[23] P. Warnitchai, T. Pinkaew, Modelling of liquid sloshing in rectangular tanks with flow-dampening devices, Engineering Structures 20 (1998) 293-600.

[24] O.M. Faltinsen, R. Firoozkoohi, A.N. Timokha, Analytical modeling of liquid sloshing in a two-dimensional rectangular tank with a slat screen, Journal of Engineering Mathematics 70 (2011) 93-109.

[25] J. Hamelin, J. Love, M. Tait, J. Wison, Tuned liquid dampers with a Keulegan-Carpenter number-dependent screen drag coefficient, Journal of Fluids and Structures 43 (2013) 271-286.

[26] M.J. Tait, Modelling and preliminary design of a structure-TLD system, Engineering Structures. 30 (2008) 2644-2655.

[27] W.H. Tsao, W.S. Hwang, Tuned liquid dampers with porous media, Ocean Engineering 167 (2018) 55-64.

[28] W.H. Tsao, W.S. Hwang, Dynamic characteristics of liquid sloshing in cylindrical tanks filled with porous media. Earth and Environmental Science 351 (2019).

[29] W.H. Tsao, T.J. Chang, Sloshing phenomenon in rectangular and cylindrical tanks filled with porous media: supplementary solution and impulsive-excitation experiment, Journal of Engineering Mechanics 146 (2020) 04020139.

[30] W.H. Tsao, Y.L. Huang, Sloshing force in a rectangular tank with porous media, Results in Engineering 11 (2021) 100250.

[31] W.H. Tsao, L.H. Huang, W.S. Hwang, An equivalent mechanical model with nonlinear damping for sloshing rectangular tank with porous media, Ocean Engineering, 242 (2021) 110145.

[32] S.T. Grilli, J. Skourup, I.A. Svendsen, An efficient boundary element method for nonlinear water waves, Engineering Analysis with Boundary Elements 6(2) (1989) 97-107.

[33] S.T. Grilli, J. Horrillo, Numerical generation and absorption of fully nonlinear periodic waves, Journal of Engineering Mechanics 123(10) (1997) 1060-1069.

[34] D. Sen, Numerical simulation of motions of two-dimensional floating bodies, Journal of Ship Research 37(4) (1993) 307-30.

[35] E.F.G. Van Daalen, Numerical and theoretical studies of water waves and floating bodies. PhD thesis (1993) Universiteit Twente, The Netherlands.

[36] K. Tanizawa, A nonlinear simulation method of 3D body motions in waves, Journal of the Society of Naval Architects of Japan 178 (1995) 179-191.

[37] A.J. Hermans, A boundary element method for the interaction of free-surface waves with a very large floating flexible platform, Journal of Fluids and Structures 14 (2000) 943-956.

[38] W. Koo, M.H. Kim, Freely floating-body simulation by a 2D fully nonlinear numerical wave tank, Ocean Engineering 31(16) (2004) 2011-46.

[39] K.H. Jung, K.A. Chang, H.J. Jo, Viscous effect on the roll motion of a rectangular structure, Journal of Engineering Mechanics 132(2) (2006) 190-200.

[40] Y. Kim, B.W. Nam, D.W. Kim, Y.S. Kim, Study on coupling effects of ship motion and sloshing, Ocean Engineering 34(16) (2007) 2176-2187.

[41] E. Guerber, M. Benoit, S.T. Grilli, C. Buvat, A fully nonlinear implicit model for wave interactions with submerged structures in forced or free motion, Engineering Analysis with Boundary Elements 36 (2012) 1151-1163.

[42] E. Dombre, M. Benoit, D. Violeau, C. Peyrard, S.T. Grilli, Simulation of floating structure dynamics in waves by implicit coupling of a fully non-linear potential flow model and a rigid body motion approach, Journal of Ocean Engineering and Marine Energy 1 (2015) 55-76.

[43] T. Vinje, P. Brevig, Nonlinear, two-dimensional ship motions, Technical Report of the Norwegian Institute of Technology (1981) R-112.81.

[44] K.A. Belibassakis, A boundary element method for the hydrodynamic analysis of floating bodies in variable bathymetry regions, Engineering Analysis with Boundary Elements 32(10) (2008) 796-810.

[45] G.X. Wu, R. Eatock-Taylor, Transient motion of a floating body in steep water waves, Proceedings of the 11th international workshop on water waves and floating bodies (1996) Hamburg, Germany.

[46] S. Piperno, C. Farhat, B. Larrouturou, Partitioned procedures for the transient solution of coupled aroelastic problems Part I: model problem, theory and two-dimensional application, Computer Methods in Applied Mechanics and Engineering 124(1-2) (1995) 79-112.

[47] C. Farhat, M. Lesoinne, Two efficient staggered algorithms for the serial and parallel solution of three-dimensional nonlinear transient aeroelastic problems, Computer Methods in Applied Mechanics

and Engineering 182(3-4) (2000) 499-515.

[48] J.L. Guermond, P. Minev, J. Shen, An overview of projection methods for incompressible flows, Computer Methods in Applied Mechanics and Engineering 195(44-47) (2006) 6011-6045.

[49] H.G Matthies, R. Niekamp, Jan Steindorf, Algorithms for strong coupling procedures, Computer Methods in Applied Mechanics and Engineering 195 (2006) 2028-2049.

[50] M.V. Rodrigues, F.N. Correa, B.P. Jacob, Implicit domain decomposition methods for coupled analysis of offshore platforms, Communications in Numerical Methods in Engineering 23 (2007) 599-621.

[51] J. Palm, C. Eskilsson, G.M. Paredes, L. Bergdahl, Coupled mooring analysis of floating wave energy converters using CFD: Formulation and Validation, International Journal of Marine Energy 16 (2016) 83-99.

[52] T.E. Tezduyar, Finite element methods for flow problems with moving boundaries and interfaces, Computational Methods in Engineering 8 (2001) 83-130.

[53] M. Karimirad, C. Michailides, A. Nematbakhsh, Offshore Mechanics: Structural and Fluid Dynamics for Recent Applications (2018) Wiley, UK.

[54] S. Osher, J.A. Sethian, Fronts propagating with curvature-dependent speed: algorithms based on hamilton-jacobi formulations, Journal of Computational Physics 79 (1988) 12-49.

[55] S. Osher, R. Fedkiw, Level set methods and dynamic implicit surfaces, Applied Mathematical Sciences 153 (2003) Springer-Verlag, New York.

[56] R. Mittal, G. Iaccarino, Immersed boundary methods, Annual Review of Fluid Mechanics 37(1) (2005) 239-261.

[57] Proteus: Computational Methods and Simulation Toolkit, http://proteustoolkit.org

[58] A. Tasora, R. Serban, H. Mazhar, A. Pazouki, D. Melanz, J. Fleischmann, M. Taylor, H. Sugiyama, D. Negrut, Chrono: An open source multi-physics dynamics engine, High Performance Computing in Science and Engineering - Lecture Notes in Computer Science (2016) Springer.

[59] A.D. Nield, A. Bejan, Convection in porous media, 4th ed., (2013) New York, Springer.

[60] J.C. Ward, Turbulent flow in porous media, ASCE Journal of the Hydraulics Division 90 (1964) 1-12.

[61] G.S. Beavers, D.D. Joseph, Boundary conditions at a naturally permeable wall, Journal of Fluid Mechanics 30 (1967) 197-207.

[62] W.L. Brogan, Modern Control Theory, 3rd ed., (1991) Prentice Hall, New Jersey.

[63] Y. Bazilevs, V. Calo, J. Cottrel, T. Hughes, A. Reali, G. Scovazzi, Variational multiscale residual-based turbulence modeling for large eddy simulation of incompressible flows, Computer Methods in Applied Mechanics and Engineering 197 (2007) 173-201.

[64] C.E. Kees, I. Akkerman, M.W. Farthing, Y. Bazilevs, A conservative level set method suitable for variable-order approximations and unstructured meshes, Journal of Computational Physics 230 (2011) 4536-4558.

[65] C.S. Peskin, Numerical analysis of blood flow in the heart, Journal of Computational Physics 25(3) (1977) 220-252.

[66] F. Ursell, R.G. Dean, Y.S. Yu, Forced small-amplitude water waves: a comparison of theory and experiment, Journal of Fluid Mechanics 7(1) (1960) 33-52.

[67] N.G. Jacobsen, D.R. Fuhrman, J. Fredsøe, A wave generation toolbox for the open-source CFD library: OpenFoam, International Journal for Numerical Methods in Fluids 70 (2012) 1073-1088.

[68] J.P. Den Hartog, Mechanical Vibrations, fourth ed. (1956) McGraw-Hill, New York.

[69] T.T. Soong, G.F. Dargush, Passive Energy Dissipation Systems in Structural Engineering (1997) Wiley, New York.